ACS APPLIED ENERGY MATERIALS

Amorphous Metal−Organic Framework-Coated Halloysite Nanotubes as Efficient Sulfur Immobilizers for Lithium−Sulfur Batteries

Published as part of ACS Applied Energy Materials special issue "70th Anniversary of Materials Science at Donghua University".

Sijia Cao,[#] Meltem Karaismailoglu Elibol,[#] Yael Rodriguez Ayllon,[#] Qingping Wu, Johannes Schmidt, Wei Zhang,* and Yan Lu*

Cite This: *ACS Appl. Energy Mater.* 2025, 8, 9646−9655 Read Online

ACCESS | Metrics & More | Article Recommendations | Supporting Information

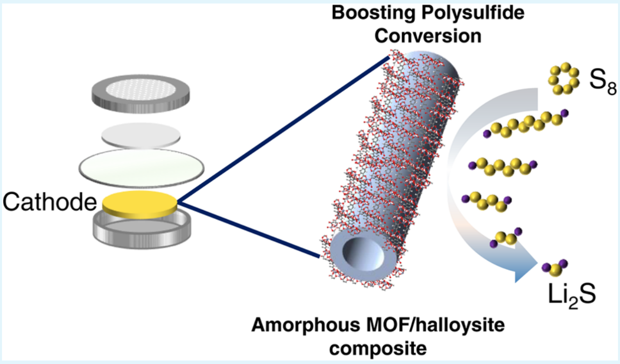

ABSTRACT: Lithium−sulfur (Li−S) batteries, known for their high theoretical energy density, have been considered as one of the most promising candidates for next-generation batteries. However, further optimization of their electrochemical performance is often hindered by a sluggish polysulfide conversion process. Recently, amorphous metal−organic frameworks (aMOFs) with numerous unsaturated metal sites have emerged as efficient catalysts, particularly in boosting polysulfide conversion. However, the collapse of the long-range periodic porous structure makes it difficult to access the internal part of micrometer-sized aMOFs, thereby limiting the further improvement of their catalytic activity. Herein, we propose a promising core−shell structure, constructed by using a sustainable halloysite nanotube as a substrate to support aMOF. The triethylamine vapor diffusion method is applied to regulate the kinetics of aMOF growth by modulating the deprotonation of organic ligands, leading to the successful deposition of nanosized aMOF shells onto halloysite nanotubes. This aMOF/halloysite composite structure exhibits better catalytic activity toward polysulfide adsorption and conversion in the Li−S battery when compared with the pure halloysite. In addition, the composite also shows a better cycling performance, retaining a specific capacity of 510 mAh g^{-1} after 350 cycles at 1.0 C. This work presents an efficient amorphous MOF shell-coating structure as a catalyst in facilitating the process of polysulfide conversion, paving the way for the development of highly active aMOF-based catalysts in the future.

KEYWORDS: *amorphous, metal−organic framework, Li−S battery, halloysite nanotube, sulfur cathode*

INTRODUCTION

The increase in demand for high-performance energy storage systems is one of the major reasons for intensified research in battery technology.[1] Lithium−sulfur (Li−S) batteries, with their exceptionally high theoretical energy density of 2600 Wh kg^{-1} and the natural abundance of sulfur, possess a promising potential for being an alternative to conventional lithium-ion batteries.[2,3] However, the commercialization of Li−S batteries is hindered by several challenges, such as poor electrical conductivity of sulfur,[4] volume expansion of cathode material,[5] and particularly the dissolution of lithium polysulfides (LiPSs), causing the shuttle effect during the cycling process.[6] Advanced cathode materials development with enhanced conductivity and polysulfide-confining capability can assist in overcoming these issues.[7,8] There are three strategies to improve the battery's performance through the development of cathode host materials: adsorption or encapsulation of lithium polysulfide, the utilization of redox mediators, and catalysts.[9] Encapsulation of sulfur with highly conductive carbon nanotubes (CNTs) and nitrogen-doped graphene is a method to enhance the sulfur loading. However, their nonpolar nature prevents sufficient trapping of polar LiPSs. Hence, polar host materials are more functional for the adsorption of the LiPSs via strong chemical bonds.[10] Metal-based compounds integrated into the sulfur cathode can be functionalized as redox mediators by lowering charge-transfer resistance and facilitating LiPSs conversion by enabling a new reaction

Received: April 30, 2025
Revised: June 6, 2025
Accepted: June 9, 2025
Published: June 16, 2025

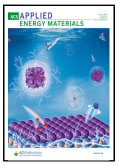

https://doi.org/10.1021/acsaem.5c01276

Scheme 1. (a) Schematic Illustration of Top-Down Method for Fabrication of Amorphous MOFs. (b) Schematic Illustration of Vapor Diffusion Method for the Bottom-Up Assembly of Amorphous MOFs onto Halloysite and Their Application in Facilitating the Polysulfide Conversion

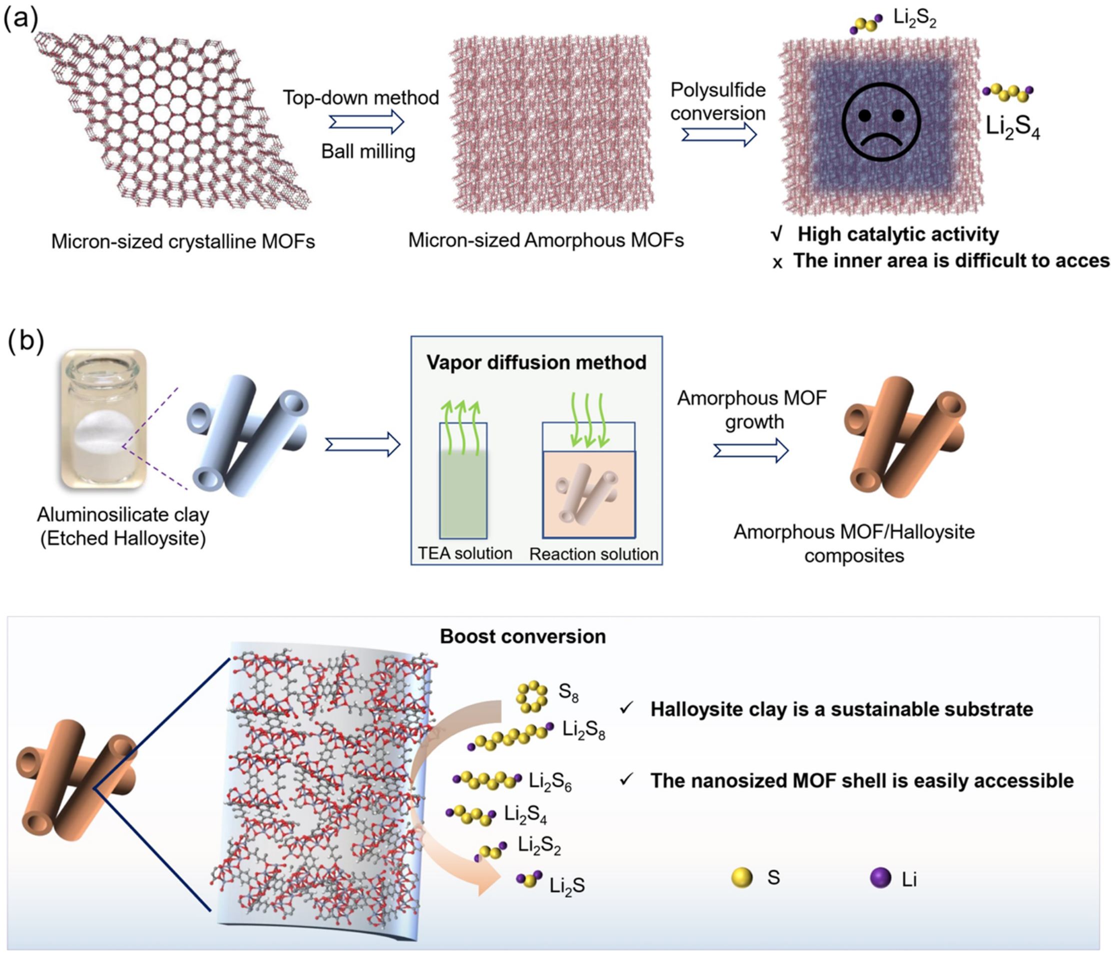

pathway alongside the conventional $S_8 \leftrightarrow$ LiPSs $\leftrightarrow Li_2S_2/Li_2S$ pathway.[11,12] Furthermore, polar metal-based compounds as host materials with strong chemisorption abilities are utilized as electrocatalysts to suppress the shuttle effect effectively.[10,13−17]

Metal−organic frameworks, as a subset of crystalline coordination polymers, are periodically constructed from metal-based nodes and organic linkers.[18,19] Owing to their interconnected porous structure and customized chemical properties, they have been extensively studied for applications in gas adsorption and separation,[20,21] energy storage,[22−24] sensing,[25] and catalysis.[26,27] Notably, the abundance of open metal sites within their frameworks confers exceptional catalytic properties for a wide range of reactions, including organic synthesis,[28,29] water splitting,[30] and CO_2 reduction.[31] Among them, highly crystalline MOFs with impressive catalytic activity have been used as sulfur hosts or separator modulators in lithium−sulfur batteries to mitigate the shuttle effect by enhancing polysulfide conversion.[32−34] Recently, amorphous metal−organic frameworks (aMOFs), as a unique material form, have attracted increasing interest due to their distinctive characteristics compared to crystalline forms,[35−44] including enhanced conductivity,[35] tunable drug delivery,[36] and improved gas separation capability.[37,38] Notably, the missing organic linkers and long-range disordered structure within the amorphous framework intrinsically induce the formation of abundant unsaturated metal sites with high activity.[45−47] Furthermore, amorphous MOFs can form more uniform heterogeneous structures within composite systems, thereby effectively enhancing catalytic activity.[48] This structural feature enhances their catalytic performance in many reaction systems, especially in polysulfide conversion.[49−51] However, amorphous MOFs are generally characterized by micrometer-scale or larger particle sizes (Scheme 1a). The disordered and collapsed pore structure prevents polysulfides from accessing the internal regions, limiting the effective utilization of these areas.

Considering this limitation of amorphous MOFs in Li−S batteries, the coating of halloysite nanotubes (HNTs) with amorphous MOFs as a composite sulfur host has been proposed for better battery performance. Halloysite is a naturally occurring, low-cost clay mineral and possesses distinct advantages from counterparts like montmorillonite (MMT), vermiculite (VR), and sepiolite (SEP).[52] Unlike the other clays with planar or fibrous morphologies, HNTs possess a 1D tubular structure formed by rolled 1:1 aluminosilicate layers. Its unique geometry provides an internal hollow lumen, allowing effective physical confinement of sulfur species and accommodating their volumetric changes during cycling. Furthermore, mesoporous halloysite nanotubes possess a high surface area and intrinsic polarity (Si−OH and Al−OH functional groups), which offer notable advantages in sulfur dispersion uniformity and in facilitating the transport of lithium ions, electrons, and polysulfide anions.[52−54] Layered mineral, such as MMT, which is studied to modify the separator or serve as a sulfur carrier in Li−S batteries, is prone to structural instability under prolonged cycling. Compared to that, HNTs demonstrate better mechanical robustness and a more stable porous framework.[55] Additionally, recent studies demonstrate the effectiveness of nanotubular or monolithic holey structures for sulfur hosts to enhance conductivity, catalytic activity, and polysulfide confinement in Li−S batteries. These advanced architectures highlight the importance of tubular and porous designs, as naturally embodied by HNTs.[56−58] However, halloysite exhibits limited catalytic activity in polysulfide conversion, restricting its application in Li−S batteries. Amorphous MOFs have the potential to enhance this catalytic activity, while mesoporous halloysite can address the inadequate porosity of MOFs as sulfur cathodes. Therefore, the development of a composite structure combining amorphous MOFs with halloysite nanotubes presents a promising strategy for sulfur host materials.

Herein, we propose a sustainable halloysite-supported amorphous MOF composite structure as a sulfur host in Li−S batteries. Compared to the top-down amorphization methods in previous reports, the kinetics-controlled bottom-up assembly method is utilized in this work to construct the nanosized amorphous MOF-coated halloysite composite structure, leveraging the structural advantages of both materials. Briefly, triethylamine (TEA) vapor as a weak organic base source is used to modulate the pH of the reaction solution, and then regulate the deprotonation process of organic ligand (Scheme 1b).[43,59] This heteronucleation of complexation between deprotonated ligands and metal ions tends to occur on the surface of HNTs, leading to the deposition of aMOF onto HNTs. The nanotubular morphology of HNTs increases the ability of LiPS confinement, while the nanosized amorphous MOF matrix provides redox-active sites to accelerate sulfur conversion kinetics (Scheme 1b). This study highlights the potential of the aMOF/HNT composite as an efficient cathode host material for Li−S batteries.

■ EXPERIMENTAL METHODS

Materials and Reagents. Esan Eczacıbaşı Industrial Raw Materials Company supplied halloysite. Sulfuric acid (H_2SO_4, 98%), 2,5-dihydroxyterephthalic acid, iron(II)-chloride tetrahydrate ($FeCl_2 \cdot 4H_2O$), anhydrous ethanol, methanol, triethylamine (TEA), lithium nitrate ($LiNO_3$, 99.99%), bis(trifluoromethane) sulfonimide lithium salt (LiTFSI, anhydrous, 99.99%), *N*-methyl-2-pyrrolidone (NMP, anhydrous, 99.5%), polyvinylidene fluoride (PVDF), 1,3-dioxolane (DOL, anhydrous, 99.8%), 1,2-dimethoxyethane (DME, anhydrous, 99.5%), and sulfur powder were purchased from Sigma−Aldrich. All reagents were utilized without any further treatments or purifications.

Preparation of Acid-Treated Halloysite Nanotubes (HNTs). The halloysite powder (1 g) was etched in sulfuric acid solution (100 mL, 1 mol L^{-1}) as described in our previous study.[52] After the HNTs were pretreated in the sulfuric acid solution at 50 °C overnight, they were washed with distilled water three times.

Synthesis of Amorphous MOF/HNT (aMOF/HNT). aMOF/HNT was synthesized by using the diffusion technique. First, a ligand solution (5 mg mL^{-1}) was prepared by dissolving 2,5-dihydroxyterephthalic acid in methanol, and then an aqueous solution of $FeCl_2 \cdot 4H_2O$ (200 mg mL^{-1}) was prepared as the metal precursor. To form the reaction solution in a vial, 0.53 mL of ligand solution (5 mg mL^{-1}) diluted in 4.5 mL of methanol and 30 μL of aqueous $FeCl_2$ solution (200 mg mL^{-1}) were added to the 10 mg etched HNTs dispersed in 5 mL of methanol. In the second vial, a triethylamine (TEA) solution was prepared by adding 1 mL of TEA in 10 mL of ethanol. Then, the reaction solution and TEA solution that were prepared in the uncapped vials were placed into a beaker. The beaker was sealed, and the reaction solution was stirred at room temperature. During this process, the volatilized TEA slowly diffused into the reaction solution. The amorphous MOF/HNT was collected after 2.5 h and washed with ethanol three times by centrifugation.

Characterization. X-ray diffraction (XRD) patterns were collected in a Bruker D8 diffractometer in locked-coupled mode with Cu Kα1 radiation (wavelength of 1.5406 Å). X-ray photoelectron spectroscopy (XPS) was performed using a Thermo Scientific K--Alpha X-ray Photoelectron Spectrometer with Al Kα radiation. The samples were mounted on a sample holder with carbon tape for analysis. Fourier transform infrared (FTIR) spectra were acquired by using a Thermo Nicolet Magna 750 FTIR Spectrometer with KBr pressing for powder samples. The nitrogen adsorption−desorption isotherms were collected in a Quantachrome Autosorb-1 system performed at 77 K. The Brunauer−Emmett−Teller (BET) method was used to calculate the specific surface area based on a multipoint analysis. The aMOF content in the aMOF/HNT composite and the sulfur content in the aMOF@HNT/S were determined through thermogravimetric analysis (TGA) in a Netzsch TG 209F1 Iris under Ar (or synthetic air). The analysis was conducted at a heating rate of 10 °C min^{-1}, scanning from room temperature to 700 °C. The Raman spectra were recorded using an XPLORA Plus Raman microscope equipped with a 532 nm laser. The nanostructure of the synthesized samples was recorded by using a LEO 1530 field-emission SEM and an FEI Talos F200S transmission electron microscope (TEM). The elemental composition analysis of the samples was determined by using energy-dispersive X-ray spectroscopy (EDX) with two silicon drift detectors (SDD).

Electrochemical Tests. The HNTs/S or aMOF/HNT/S composites were prepared by mixing the HNTs or aMOF/HNT powder with sulfur in a weight ratio of 2:8 by a thermal diffusion method at 155 °C. The HNTs/S or aMOF/HNT/S composites were mixed with super P and polyvinylidene fluoride (PVDF) in a weight ratio of 7:2:1 in the *N*-Methyl-2-Pyrrolidone (NMP) solvent to prepare the uniform slurry. The slurry was coated onto carbon paper using a doctor blade and dried in an oven at 50 °C for 12 h. The electrode was then cut into round slices with a diameter of ∼12 mm as cathodes. The areal loading of active materials is ∼1.6−2.0 mg cm^{-2}. The CR2025-type coin cells were assembled with the cathode, a Li chip as the anode, and a piece of Celgard 2500 membrane as the separator in an Ar-filled glovebox (UNIlab plus, M. BRAUN) with H_2O content <0.5 ppm and O_2 content <0.5 ppm. 1 M LiTFSI dissolved in 1,2-dimethoxyethane (DME)/1,3-dioxolane (DOL) (v/v = 1:1) with 2 wt % $LiNO_3$ was prepared as the electrolyte. The volume of the electrolyte for each cell is 40 μL. The current density of 1 C equals 1672 mA g^{-1}. Galvanostatic (dis)charging tests were performed on a Neware battery testing system (CT-4008-5 V10 mA) at room temperature. The electrochemical impedance spectroscopy (EIS) was recorded using a GAMRY Interface 1000 within a frequency range of 100 kHz to 0.01 Hz. The cyclic voltammetry (CV) was performed with the GAMRY Interface 1000 instrument in the electrochemical window of 1.7−2.8 V vs Li/Li^+. A Li_2S_6 solution was prepared by dissolving stoichiometric sulfur and Li_2S (5:1, in molar ratio) in a mixed DOL/DME (1:1, v/v), followed by vigorous stirring at 80 °C for 48 h. A Li_2S_8 solution was prepared by using the same procedure with sulfur and Li_2S in a 7:1 molar ratio. For the static polysulfide adsorption test, 10 mg of HNTs or aMOF/HNT powder was added to 4 mL of a 1 mM Li_2S_6 solution. The mixture was placed in a glovebox and allowed to stand for 10 h. Afterward, the solution was centrifuged and the supernatant was collected for UV−vis absorption analysis. For the polysulfide conversion tests, the slurry of the host materials (HNTs or aMOF/HNTs), super P, and PVDF (70:20:10 wt %) in NMP was coated on carbon paper. After being dried at 50 °C overnight, the electrode was cut into slices with a diameter of ∼12 mm. The areal loading of the host materials was ∼0.8 mg cm^{-2}. Two identical electrodes were used to assemble the symmetric cells. A 40 μL 0.1 M Li_2S_6 solution with 1.0 M LiTFSI dissolved in DOL/DME (1:1, v/v) solvent with 2 wt % $LiNO_3$ was

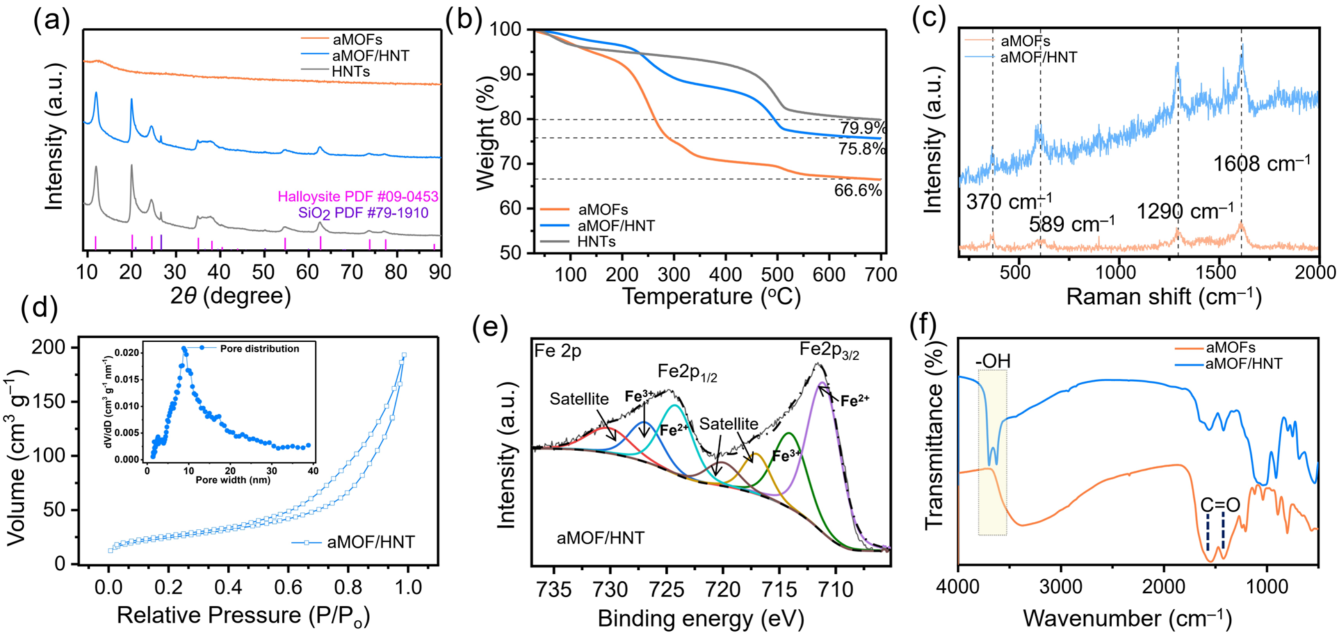

Figure 1. (a) PXRD patterns of pure aMOFs, aMOF/HNT, and HNTs samples. (b) TGA curves of pure aMOFs, aMOF/HNT, and HNTs samples measured under air flow from room temperature to 700 °C. (c) Raman spectra of aMOFs and aMOF/HNT. (d) N_2 adsorption/desorption isotherms of the aMOF/HNT composite. The inset figure shows the corresponding pore size distribution. (e) High-resolution XPS Fe 2p spectrum of aMOF/HNT composite. (f) FTIR spectra of aMOFs and aMOF/HNT composites.

used as electrolyte. The symmetric cells were measured at a scan rate of 3.0 mV s^{-1} in a potential window of −0.8 to 0.8 V. The same electrodes were used in the Li_2S precipitation tests. The cells were assembled using 20 μL of 0.25 M Li_2S_8 solution with 1.0 M LiTFSI in DOL/DME (1:1, v/v) solvent with 2 wt % $LiNO_3$ as catholyte, and 20 μL of electrolyte without Li_2S_8 was used as anolyte. The cells were first galvanostatically discharged at 0.05 C to 2.16 V and then potentiostatically held at 2.05 V for Li_2S nucleation and growth.

■ RESULTS AND DISCUSSION

Sustainable and environmentally benign halloysite clay ($Al_2Si_2O_5(OH)_4{\cdot}2H_2O$) was used as a substrate to support amorphous MOFs.[52] Halloysite nanotubes, which naturally have a hollow tubular structure, were structurally modified through an acidic etching process. $FeCl_2$ as a metal precursor and H_4dobdc (dobdc^{4-} = 2,5-dioxido-1,4-benzenedicarboxylate) as an organic linker were selected to construct the coordination framework. As shown in Scheme 1b, the amorphous Fe-MOFs/halloysite (aMOF/HNT) composite was synthesized using the triethylamine (TEA) vapor diffusion method.[43,59] TEA vapor, as a weak base, gradually generates and diffuses into the reaction solution to regulate the deprotonation rate of H_4dobdc. When the monomer concentration reaches the threshold, heterogeneous nucleation of the amorphous MOFs occurs on the surface of the halloysite nanotube, followed by stepwise growth around it through the continuous formation of the Fe-dobdc coordination framework, ultimately resulting in the formation of an amorphous Fe-MOF/halloysite composite. The initial pH of the reaction solution was 6.22. After TEA vapor diffusion, the pH increased to 8.02, demonstrating that the gradual introduction of TEA vapor slowly increased the solution pH and facilitated the deprotonation process. The driving force for heterogeneous nucleation lies in the lower energy barrier for nucleation on solid surfaces compared to homogeneous nucleation in the liquid phase. Unlike the conventional nucleation−growth process, the introduction of TEA vapor enables the gradual release of deprotonated ligands during the reaction process, thereby facilitating the heterogeneous surface nucleation and controlled growth of amorphous MOF around the substrate. In addition, pure amorphous Fe-MOF was synthesized without halloysite and was used for comparison.

The amorphous nature of Fe-MOF within the composite was confirmed by Powder X-ray diffraction (PXRD) patterns. In Figure 1a, all peaks in the aMOF/HNT match well with those of pure HNTs, without any impurity peaks from the MOF, indicating the absence of long-range order within the MOF. These results are consistent with those of pure amorphous MOF, which only shows a broad peak. Thermogravimetric analysis (TGA) was performed under a synthetic air atmosphere to determine the decomposition profile of the aMOF/HNT composite. In Figure 1b, the TGA curve of the aMOF/HNT exhibits a combination of weight loss behaviors observed in both pure aMOFs and HNTs. Below 400 °C, the major decomposition event corresponds to the breakdown of the organic framework, while another significant weight loss around 500 °C is attributed to the removal of lattice water within the HNTs. The aMOF content in the aMOF/HNT composite can be calculated from the TGA curves to be 44 wt %.

Fourier transform infrared (FTIR) and Raman spectroscopy were also used to confirm the presence of the amorphous MOFs within the composite. In Figure 1c, the Raman spectra of the aMOF/HNT composite display patterns identical to those of the pure MOFs. The peak observed at 589 cm^{-1} is attributed to the bending and deformation vibrations of the benzene ring. Additionally, the band near 370 cm^{-1} may correspond to the ν(Fe−O) vibrational mode. The two extra peaks at 1290 and 1608 cm^{-1} are attributed to the organic ligand within MOF, including symmetric stretching ν(COO$^-$), ν(C−O), and stretching/deformation vibrations of benzene.[60] Furthermore, the FTIR spectra of the aMOF/HNT composite

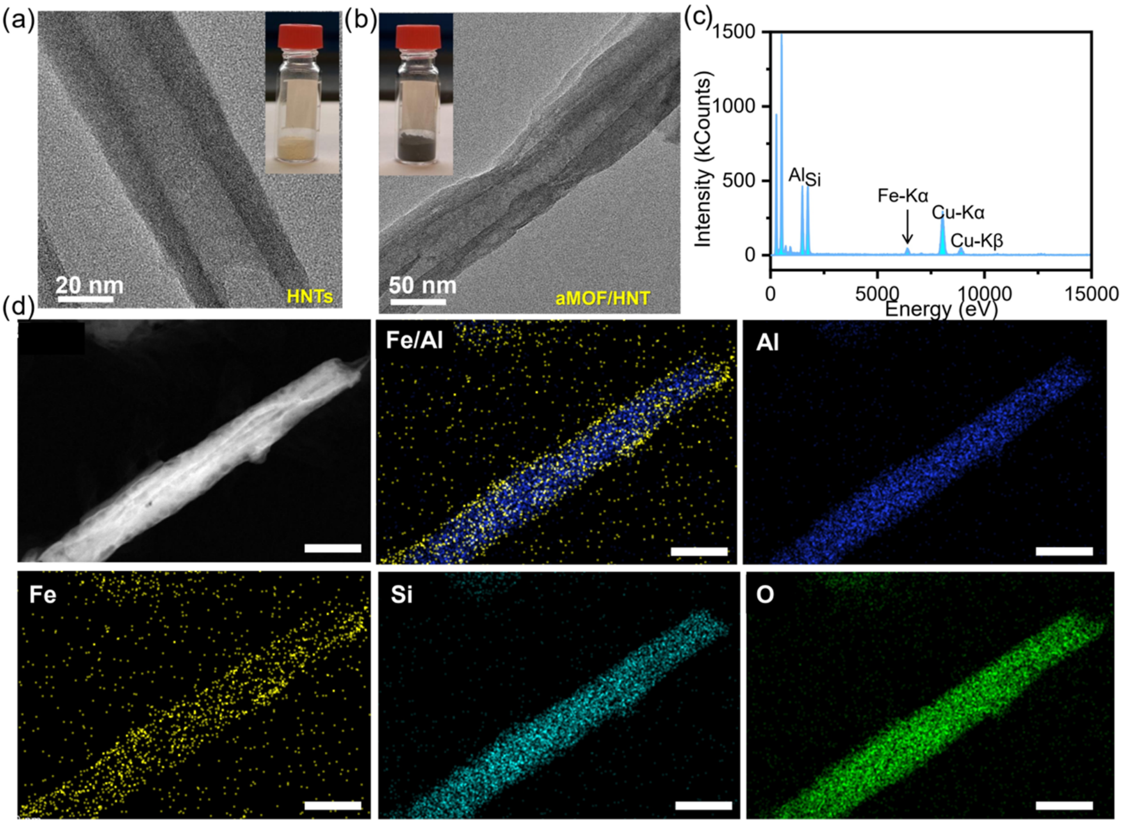

Figure 2. TEM images of (a) etched HNTs and (b) aMOF/HNT. Inset is a photo of the corresponding powder materials. (c) Energy-dispersive X-ray analysis (EDX) spectrum of aMOF/HNT. (d) Element mapping images of aMOF/HNT. The scale bar is 100 nm.

also exhibit a pattern similar to that of pure MOFs (Figure 1f). The two peaks at 1570 and 1415 cm^{-1} are assigned to the vibrations and asymmetric stretching of the C═O bonds in $dobdc^{4-}$.[61] Notably, the peaks around 3600 cm^{-1} observed in the composite can be attributed to hydroxyl (−OH) groups, originating from the HNTs.[62] Figures 1d and S1 show the N_2 adsorption−desorption isotherms of aMOF/HNT composite, pure aMOFs, and HNTs. The calculated Brunauer−Emmett−Teller (BET) specific surface areas are 87, 9, and 118 m^2/g, respectively. The amorphous nature, which induces the collapse of the framework, results in a low specific surface area of the amorphous MOFs. The mesoporous structure of the aMOF/HNT composite, with pore sizes of around 10 nm, originates from the hollow tubular structure of the halloysite. These results indicate that the initial porous structure of HNTs remained unchanged during the coating process. The presence of Fe(III) on the surface of the aMOF/HNT composite is confirmed by X-ray photoelectron spectroscopy (XPS). The two peaks at 713.8 and 726.7 eV correspond to Fe^{3+} $2p_{3/2}$ and Fe^{3+} $2p_{1/2}$, respectively (Figures 1e and S2).[63] This oxidation occurs during the formation of the amorphous framework, consistent with previous reports.[63]

The results presented above clearly confirm the successful synthesis of the aMOF/HNT composite. To further investigate the distribution of the amorphous metal−organic framework within the composite structure, scanning electron microscopy (SEM), transmission electron microscopy (TEM), and energy-dispersive X-ray spectroscopy (EDX) were employed for detailed characterization. Pure halloysite exhibits an obvious hollow tubular structure with around 800 nm in length and 15 nm in outer diameter (Figures 2a and S3a). After the amorphous MOF growth, the white halloysite powder turned black and the surface of the tubes became rougher (Figure 2b), while maintaining the initial tube structure (Figure S3b). Additionally, in Figure 2c, EDX elemental analysis clearly shows the presence of Fe, Al, and Si within the composite. Fe originates from Fe-MOF, while Al and Si are derived from halloysite. Furthermore, in the elemental mapping images, Fe is uniformly distributed on the surface of the halloysite (Figures 2d and S4−S5), confirming the successful growth of the amorphous MOF on the HNTs surface, forming a core−shell structure of aMOF/HNT composite. To confirm the role of TEA vapor, we conducted a control experiment without the addition of TEA vapor. The elemental mapping images indicate that an amorphous MOF does not form on the HNT surface (Figure S6), which is due to the inhibition of the deprotonation process.

The polysulfide adsorption capability was evaluated by immersing the HNTs and aMOF/HNT powders in 1 mM Li_2S_6 solutions, respectively. After 10 h, both solutions containing HNTs and aMOF/HNT became nearly colorless (Figure 3a). The corresponding UV−vis absorption spectra also show similar adsorption capabilities for these two materials, indicating that the adsorption behavior primarily originates from the HNTs. The electrocatalytic activity of HNTs and aMOF/HNT toward LiPSs conversion was assessed using symmetric cells with a Li_2S_6 electrolyte. As shown in Figure 3b, the weak current response from the HNTs electrode indicates that it shows no significant catalytic effect on the LiPSs conversion.[64] In contrast, the aMOF/HNT electrodes exhibit a much more pronounced current response, significantly promoting the sulfur redox reaction kinetics. The

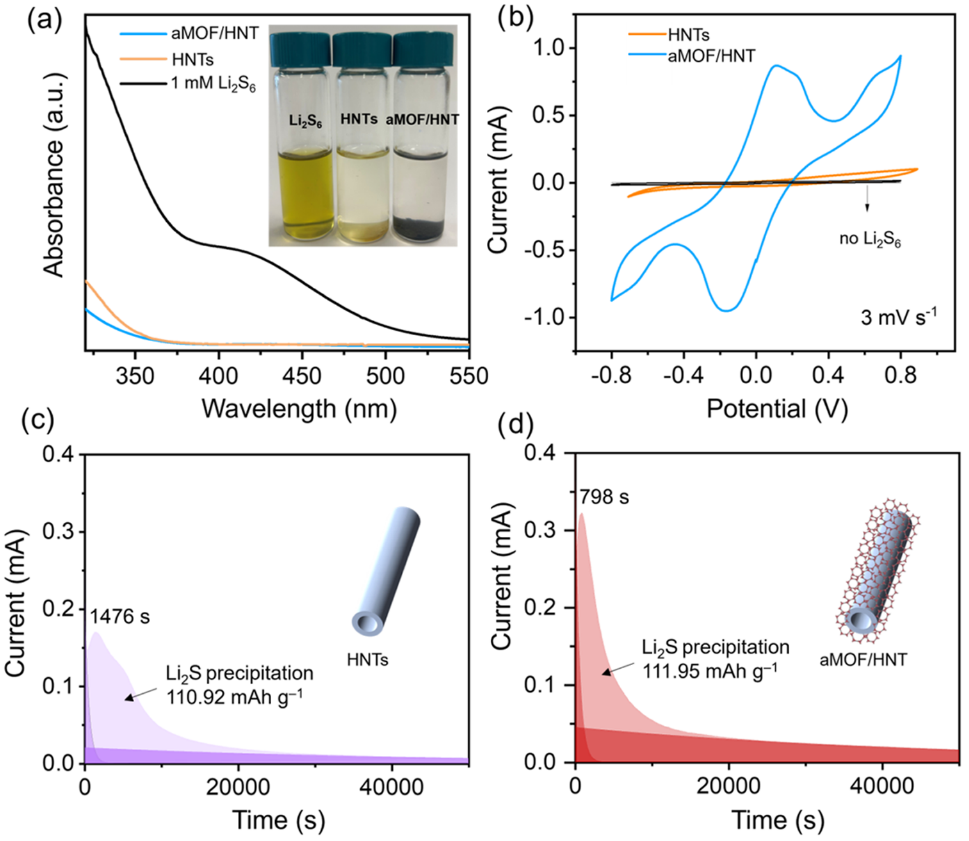

Figure 3. (a) UV−visible absorption spectra of 1 mM Li$_2$S$_6$ solution and the supernatant after adsorption test with 10 mg of HNTs and aMOF/HNT powder, respectively. Inset is the photo of Li$_2$S$_6$ solution with aMOF/HNT and HNTs after 10 h of static adsorption. (b) Cyclic voltammograms scanned at 3 mV s^{-1} of symmetric cells assembled by HNT and aMOF/HNT electrodes with Li$_2$S$_6$ electrolyte. Li$_2$S precipitation test with the Li$_2$S$_8$ catholyte of (c) HNTs and (d) aMOF/HNT electrodes, respectively.

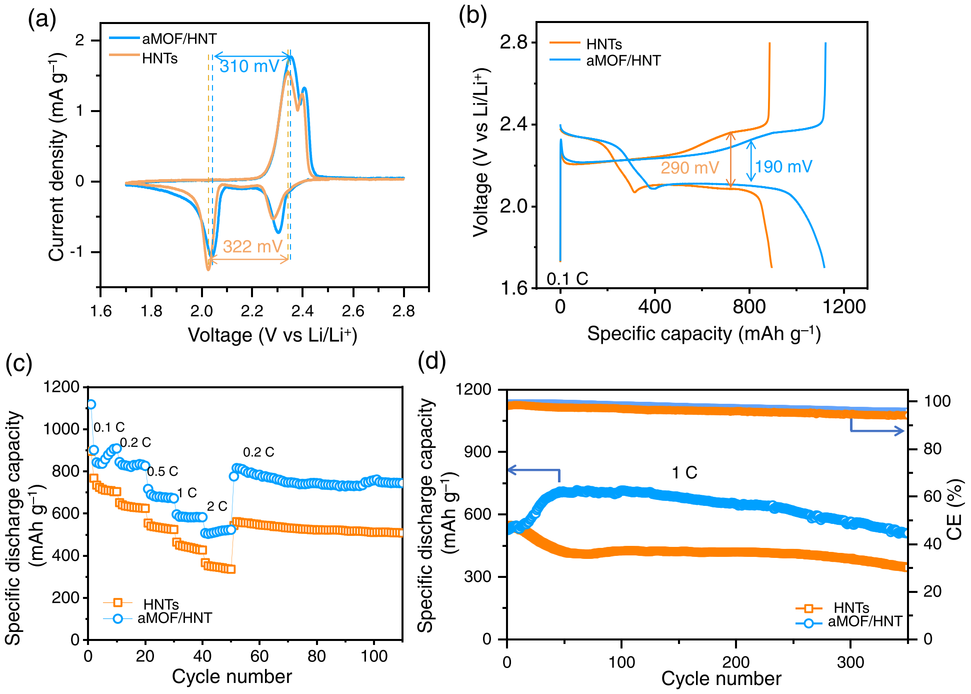

Figure 4. (a) CV of aMOF/HNT/S and HNTs/S cathodes at the scan rate of 0.1 mV s^{-1} in the potential window of 1.7−2.8 V vs Li/Li$^+$. (b) Galvanostatic (dis)charge of aMOF/HNT/S and HNTs/S cathodes at a current density of 0.1 C, respectively. (c) Rate capability at different current densities. (d) Cycling performance of aMOF/HNT/S and HNTs/S cathodes at a current density of 1.0 C over 350 cycles.

promoted kinetics of sulfur conversion on the aMOF/HNT electrodes was further verified through a Li_2S precipitation test. Figure 3c,d reveal that the Li_2S is electrodeposited more rapidly on the aMOF/HNT electrode (798 s) than on the HNTs electrode (1476 s). Despite the difference in kinetics, the similar capacity contributions observed for HNTs and aMOF/HNT can be attributed to their comparable adsorption capabilities. Therefore, the strong adsorption capability of HNTs combined with the abundant catalytic sites of aMOF jointly contribute to the enhanced electrocatalytic activity of aMOF/HNT as a sulfur host in Li−S batteries.[65]

To apply aMOF/HNT and HNTs in Li−S batteries, the aMOF/HNT/S and HNTs/S cathodes were prepared by incorporating sulfur into aMOF/HNT and HNTs at 155 °C (Figure S7), respectively. Before loading sulfur, both aMOF/HNT and HNTs undergo a degassing process under vacuum at 150 °C for 72 h to remove residual water in the HNTs. This degassing step does not alter the structure of the materials (Figures S8−S10). Electrochemical impedance spectra (EIS) (Figure S11) demonstrate a lower charge-transfer resistance of aMOF/HNT/S cathode (59 Ω) compared to that of HNT/S cathode (75 Ω), which indicates the faster interfacial reaction kinetics on aMOF/HNT electrode surface.[66] Moreover, the cyclic voltammogram (CV) (Figure 4a) of the HNTs/S display two cathodic peaks at 2.03 and 2.28 V, ascribed to the formation of long-chain LiPSs and insoluble Li_2S_2/Li_2S, respectively, and two anodic peaks at 2.34 and 2.40 V related to the reversible oxidation process.[67] aMOF/HNT/S cathode displays a similar redox behavior of elemental sulfur as well. To note, the aMOF/HNT/S cathode shows a lower voltage hysteresis (310 mV), in comparison to that of HNTs/S (322 mV), indicating the accelerated redox kinetics of sulfur redox reactions by the aMOF/HNT. The galvanostatic (dis)charge curves of aMOF/HNT/S also suggest a lower polarization (190 mV) compared to that of HNTs/S cathodes (290 mV) (Figure 4b). The rate capability of Li−S cells was evaluated at current densities ranging from 0.1 to 2.0 C and back to 0.2 C (Figure 4c). Specifically, the aMOF/HNT/S cathode exhibits specific discharge capacities of 908, 822, 686, 591, 516, and 822 mAh g^{-1} at current densities of 0.1, 0.2, 0.5, 1.0, 2.0, and 0.2 C, respectively. In comparison, the HNTs/S electrode delivers specific discharge capacities of 789, 643, 535, 444, 350, and 565 mAh g^{-1} at the corresponding current densities. These results suggest that aMOF/HNT significantly enhances sulfur utilization and accelerates the conversion kinetics of sulfur species. Moreover, the aMOF/HNT/S cathode has 70.7% capacity retention with 510 mAh g^{-1} after 350 cycles at 1.0 C, significantly outperforming the HNTs/S cathode, which shows only 63.7% retention with a specific capacity of 344 mAh g^{-1} (Figure 4d). Notably, the aMOF/HNT-based cell exhibits a gradual increase in specific capacity during the initial cycles, as shown in Figure 4c,d. This behavior can be attributed to activation of the aMOF coating during the initial sulfur redox reaction process. In Li−S batteries, cell activation is typically required to achieve full utilization of sulfur.[68] In the presence of electrocatalysts, the adsorption and subsequent conversion of sulfur species on the catalytic sites undergo a progressive activation process, which enhances their reactivity and catalytic performance. As a result, the aMOF/HNT-based cell exhibits a gradual increase in the specific capacity during the initial charge−discharge cycles, as shown in Figure 4c,d. This behavior is attributed to the ongoing activation of the aMOF coating during the early stages of the sulfur redox reactions. The cycling performance of the aMOF/HNT/S cathode at the current density of 0.2 C has also been tested, as shown in Figure S12. The Li−S coin cell delivers a discharge capacity of 819 mAh g^{-1} after the initial activation and remains at the 87.2% capacity over 100 cycles. After cyclic testing, the nanostructure of the aMOF/HNT/S showed no significant changes (Figures S13−S14), demonstrating good stability during the charge−discharge process.

CONCLUSIONS

Using the vapor diffusion method, we have achieved controlled growth of an amorphous Fe-MOF coating onto HNTs, forming an aMOF/HNT core−shell composite. TEA vapor is used to regulate the deprotonation process of H_4dobdc, thereby controlling the sol−gel process of complexation between Fe^{2+}/Fe^{3+} and deprotonated ligands of dobdc^{4-}. TEM and elemental mapping images reveal that the amorphous Fe-MOF was successfully deposited on the surface of the HNTs as a modified functional layer. Then, the obtained aMOF/HNT composite was used as a sulfur host in a Li−S battery. The aMOF/HNT-catalyzed sulfur cathode exhibited stable cycling performance, maintaining a specific capacity of 510 mAh g^{-1} over 350 cycles at 1.0 C, whereas the pure HNTs demonstrated only 63.7% capacity retention, with a remaining capacity of 344 mAh g^{-1}. Moreover, the rate capability was significantly improved with the aMOF/HNT catalysts. The enhanced electrochemical performance is attributed to the synergistic interaction within the aMOF/HNT composite: the hollow structure of HNTs serves as a physical confinement for LiPS conversion, while the aMOF shell acts as an efficient catalyst to facilitate polysulfide conversion. This work provides a new strategy for enhancing the catalytic activity of amorphous MOFs and expanding their potential applications in Li−S battery systems.

ASSOCIATED CONTENT

Supporting Information

The Supporting Information is available free of charge at https://pubs.acs.org/doi/10.1021/acsaem.5c01276.

> The supporting figures illustrate the characterization of pure aMOFs, etched HNTs, and aMOF/HNT composites; N_2 adsorption/desorption isotherms; XPS spectra of Fe_{2p} core level and the aMOF/HNT survey spectrum; SEM images of pure etched HNTs with the aMOF/HNT composite; TEM images and elemental mapping of the composite; TEM and PXRD of the structural changes in etched HNTs before and after degassing; TEM and SEM images of aMOF/HNT/S electrode before and after the cycling test; Electrochemical impedance spectra of sulfur cathodes in Li−S cells (PDF)

AUTHOR INFORMATION

Corresponding Authors

Wei Zhang − *Institute of Electrochemical Energy Storage, Helmholtz-Zentrum Berlin für Materialien und Energie, Berlin 14109, Germany*; Email: wei.zhang@helmholtz-berlin.de

Yan Lu − *Institute of Electrochemical Energy Storage, Helmholtz-Zentrum Berlin für Materialien und Energie, Berlin 14109, Germany; Institute for Technical and Environmental Chemistry, Friedrich-Schiller-Universität Jena,*

Jena 07743, Germany; Helmholtz Institute for Polymers in Energy Applications Jena (HIPOLE Jena), 07743 Jena, Germany; orcid.org/0000-0003-3055-0073;
Email: yan.lu@helmholtz-berlin.de

Authors

Sijia Cao − *Institute of Electrochemical Energy Storage, Helmholtz-Zentrum Berlin für Materialien und Energie, Berlin 14109, Germany*

Meltem Karaismailoglu Elibol − *Institute of Electrochemical Energy Storage, Helmholtz-Zentrum Berlin für Materialien und Energie, Berlin 14109, Germany; Department for Energy Science and Technology, Turkish-German University, Istanbul 34820, Turkey*

Yael Rodriguez Ayllon − *Institute of Electrochemical Energy Storage, Helmholtz-Zentrum Berlin für Materialien und Energie, Berlin 14109, Germany; Institute for Technical and Environmental Chemistry, Friedrich-Schiller-Universität Jena, Jena 07743, Germany*

Qingping Wu − *Institute of Electrochemical Energy Storage, Helmholtz-Zentrum Berlin für Materialien und Energie, Berlin 14109, Germany*

Johannes Schmidt − *Department of Chemistry, Functional Materials, Technische Universität Berlin, 10623 Berlin, Germany*

Complete contact information is available at:
https://pubs.acs.org/10.1021/acsaem.5c01276

Author Contributions

[#]The authors S.C., M.K.E., and Y.R.A. contributed equally. The manuscript was written through the contributions of all authors. All authors have given approval to the final version of the manuscript. S.C.: material characterization, data collection, and analysis. M.K.E.: material synthesis, data collection, and analysis. Y.R.A.: material characterization, data collection, and analysis. J.S. helped with XPS data collection and analysis. Q.W.: review and editing. W.Z. and Y.L.: conceptualization, data analysis, review, and editing.

Notes

The authors declare no competing financial interest.

■ ACKNOWLEDGMENTS

Q.W. acknowledges Alexander von Humboldt's research fellowship. We sincerely acknowledge Esan Eczacıbaşı Industrial Raw Materials Co. for providing the halloysite minerals. M.K.E. gratefully acknowledges the German Academic Exchange Service (DAAD) for supporting the postdoctoral fellowship. We thank J. Krone from Technische Universität Berlin for FTIR measurements.

■ REFERENCES

(1) Chatzigeorgiou, N. G.; Theocharides, S.; Makrides, G.; Georghiou, G. E. A review on battery energy storage systems: Applications, developments, and research trends of hybrid installations in the end-user sector. *J. Energy Storage* **2024**, *86*, No. 111192.

(2) Lin, S.; Wu, Q.; Lu, Y. Recent Progress of the Application of Electropolymerization in Batteries and Supercapacitors: Specific Design of Functions in Electrodes. *ChemElectroChem* **2024**, *11*, No. e202300776.

(3) Pathak, A. D.; Cha, E.; Choi, W. Towards the commercialization of Li-S battery: From lab to industry. *Energy Storage Mater.* **2024**, *72*, No. 103711.

(4) Xie, D.; Wu, Q.; Elibol, M. K.; Jiang, L.; Lu, Y. Rational designing and prospecting iron-based compounds as efficient host materials for lithium−sulfur batteries. *Curr. Opin. Green Sustainable Chem.* **2024**, *49*, No. 100958.

(5) Zhu, L.; Zhang, X.; Zhang, J.; Ren, H.; Yao, Y.; Wang, M.; Song, Y. A review on sulfur-based composite cathode materials for lithium-sulfur batteries: Progress and prospects. *J. Alloys Compd.* **2025**, *1010*, No. 178282.

(6) Du, S.; Yu, Y.; Liu, X.; Lu, D.; Yue, X.; Liu, T.; Yin, Y.; Wu, Z. Catalytic engineering for polysulfide conversion in high-performance lithium-sulfur batteries. *J. Mater. Sci. Technol.* **2024**, *186*, 110.

(7) Wu, Q.; Zhou, X.; Xu, J.; Cao, F.; Li, C. Carbon-based derivatives from metal-organic frameworks as cathode hosts for Li−S batteries. *J. Energy Chem.* **2019**, *38*, 94−113.

(8) Qiu, S.; Zhang, J.; Liang, X.; Li, Y.; Cui, J.; Chen, M. Tunable MOFs derivatives for stable and fast sulfur electrodes in Li-S batteries. *Chem. Eng. J.* **2022**, *450*, No. 138287.

(9) Ng, S.-F.; Lau, M. Y. L.; Ong, W.-J. Lithium−Sulfur Battery Cathode Design: Tailoring Metal-Based Nanostructures for Robust Polysulfide Adsorption and Catalytic Conversion. *Adv. Mater.* **2021**, *3*, No. 2008654.

(10) Yuan, B.; Hua, D.; Gu, X.; Shen, Y.; Xu, L. C.; Li, X.; Zheng, B.; Wu, J.; Zhang, W.; Li, S.; Huo, F. Polar, catalytic, and conductive $CoSe_2$/C frameworks for performance enhanced S cathode in Li−S batteries. *J. Energy Chem.* **2020**, *48*, 128.

(11) Xie, D.; Xu, Y.; Wang, Y.; Pan, X.; Härk, E.; Kochovski, Z.; Eljarrat, A.; Müller, J.; Koch, C. T.; Yuan, J.; Lu, Y. Poly (ionic liquid) nanovesicle-templated carbon nanocapsules functionalized with uniform iron nitride nanoparticles as catalytic sulfur host for Li−S batteries. *ACS Nano* **2022**, *16*, 10554−10565.

(12) Ye, H.; Lee, J. Y. Solid Additives for Improving the Performance of Sulfur Cathodes in Lithium−Sulfur Batteries—Adsorbents, Mediators, and Catalysts. *Small Methods* **2020**, *4*, No. 1900864.

(13) Zhou, Z. Q.; Wang, H. M.; Yang, L. B.; Ma, C.; Wang, J. T.; Qiao, W. M.; Ling, L. C. A review of the use of metal oxide/carbon composite materials to inhibit the shuttle effect in lithium-sulfur batteries. *New Carbon Mater.* **2024**, *39*, 201.

(14) Yan, B.; Li, X.; Xiao, W.; Hu, J.; Zhang, L.; Yang, X. Design, synthesis, and application of metal sulfides for Li-S batteries: Progress and prospects. *J. Mater. Chem. A* **2020**, *8*, 17848.

(15) Hong, X.; Wang, R.; Liu, Y.; Fu, J.; Liang, J.; Dou, S. Recent advances in chemical adsorption and catalytic conversion materials for Li−S batteries. *J. Energy Chem.* **2020**, *42*, 144.

(16) Fang, B.; Tian, X.; Wang, T.; Wang, T.; Qu, L.; Li, M. Restraining polysulfide with high-entropy metal nitride towards long cycle life and high-capacity Li−S Batteries. *ChemElectroChem* **2020**, *7*, 4737.

(17) Liu, S.; Chen, M.; Luo, Y.; He, Y.; Zhang, W.; Chen, Y.; Wang, M.; Ye, Y.; Zhu, K.; Luo, Y.; Yu, R.; Hou, J.; Liu, H.; Shu, H.; Wang, X. Synergistic electrochemical catalysis by high-entropy metal phosphide in lithium−sulfur batteries. *J. Colloid Interface Sci.* **2024**, *669*, 126.

(18) Furukawa, H.; Cordova, K. E.; O'Keeffe, M.; Yaghi, O. M. The Chemistry and Applications of Metal-Organic Frameworks. *Science* **2013**, *341*, No. 1230444.

(19) Zhou, H.-C.; Kitagawa, S. Metal−Organic Frameworks (MOFs). *Chem. Soc. Rev.* **2014**, *43*, 5415−5418.

(20) McDonald, T. M.; Mason, J. A.; Kong, X.; Bloch, E. D.; Gygi, D.; Dani, A.; Crocellà, V.; Giordanino, F.; Odoh, S. O.; Drisdell, W. S.; Vlaisavljevich, B.; Dzubak, A. L.; Poloni, R.; Schnell, S. K.; Planas, N.; Lee, K.; Pascal, T.; Wan, L. F.; Prendergast, D.; Neaton, J. B.; Smit, B.; Kortright, J. B.; Gagliardi, L.; Bordiga, S.; Reimer, J. A.; Long, J. R. Cooperative insertion of CO_2 in diamine-appended metal-organic frameworks. *Nature* **2015**, *519*, 303−308.

(21) Lin, R. B.; Xiang, S.; Zhou, W.; Chen, B. Microporous Metal-Organic Framework Materials for Gas Separation. *Chem* **2020**, *6*, 337−363.

(22) Dang, Q.; Zhang, W.; Li, Y.; Tang, L.; Hu, M. Algae-inspired multifunctional ocean solar-energy conversion chain enabled by coordination polymers. *Cell Rep. Phys. Sci.* **2021**, *2*, No. 100466.

(23) Zhang, W.; Li, Y.; Shi, C.; Qi, R.; Hu, M. Single-Crystal Lattice Filling in Connected Spaces inside 3D Networks. *J. Am. Chem. Soc.* **2021**, *143*, 6447−6459.

(24) Le, Z.; Li, W.; Dang, Q.; Jing, C.; Zhang, W.; Chu, J.; Tang, L.; Hu, M. A high-power seawater battery working in a wide temperature range enabled by an ultra-stable Prussian blue analogue cathode. *J. Mater. Chem. A* **2021**, *9*, 8685−8691.

(25) Kreno, L. E.; Leong, K.; Farha, O. K.; Allendorf, M.; Van Duyne, R. P.; Hupp, J. T. Metal−Organic Framework Materials as Chemical Sensors. *Chem. Rev.* **2012**, *112*, 1105−1125.

(26) Wei, Y. S.; Zhang, M.; Zou, R.; Xu, Q. Metal−Organic Framework-Based Catalysts with Single Metal Sites. *Chem. Rev.* **2020**, *120*, 12089−12174.

(27) Zhu, L.; Liu, X. Q.; Jiang, H. L.; Sun, L. B. Metal−Organic Frameworks for Heterogeneous Basic Catalysis. *Chem. Rev.* **2017**, *117*, 8129−8176.

(28) Yang, Q.; Xu, Q.; Jiang, H. L. Metal−organic frameworks meet metal nanoparticles: synergistic effect for enhanced catalysis. *Chem. Soc. Rev.* **2017**, *46*, 4774−4808.

(29) Shen, K.; Zhang, L.; Chen, X.; Liu, L.; Zhang, D.; Han, Y.; Chen, J.; Long, J.; Luque, R.; Li, Y.; Chen, B. Ordered macro-microporous metal-organic framework single crystals. *Science* **2018**, *359*, 206−210.

(30) Sun, K.; Huang, Y.; Sun, F.; Wang, Q.; Zhou, Y.; Wang, J.; Zhang, Q.; Zheng, X.; Fan, F.; Luo, Y.; Jiang, J.; Jiang, H.-L. Dynamic Structural Twist in Metal−Organic Frameworks Enhances Solar Overall Water Splitting. *Nat. Chem.* **2024**, *16*, 1638−1646.

(31) Kornienko, N.; Zhao, Y.; Kley, C. S.; Zhu, C.; Kim, D.; Lin, S.; Chang, C. J.; Yaghi, O. M.; Yang, P. Metal−Organic Frameworks for Electrocatalytic Reduction of Carbon Dioxide. *J. Am. Chem. Soc.* **2015**, *137*, 14129−14135.

(32) Bai, S.; Liu, X.; Zhu, K.; Wu, S.; Zhou, H. Metal−Organic Framework-Based Separator for Lithium−Sulfur Batteries. *Nat. Energy* **2016**, *1*, No. 16094.

(33) Zheng, J.; Tian, J.; Wu, D.; Gu, M.; Xu, W.; Wang, C.; Xiao, J.; et al. Lewis Acid−Base Interactions between Polysulfides and Metal Organic Framework in Lithium−Sulfur Batteries. *Nano Lett.* **2014**, *14*, 2345−2352.

(34) Li, Z.; Wang, J.; Yuan, H.; Yu, Y.; Tan, Y. Recent Progress and Challenge in Metal−Organic Frameworks for Lithium−Sulfur Battery Separators. *Adv. Funct. Mater.* **2024**, *34*, No. 2405890.

(35) Xiu, J.-W.; Wang, G.-E.; Yao, M.-S.; Yang, C.-C.; Lin, C.-H.; Xu, G. Electrical bistability in a metal−organic framework modulated by reversible crystalline-to-amorphous transformations. *Chem. Commun.* **2017**, *53*, 2479−2482.

(36) Wu, X.; Yue, H.; Zhang, Y.; Gao, X.; Li, X.; Wang, L.; Cao, Y.; Hou, M.; An, H.; Zhang, L.; et al. Packaging and delivering enzymes by amorphous metal-organic frameworks. *Nat. Commun.* **2019**, *10*, No. 5165.

(37) Wang, Y.; Jin, H.; Ma, Q.; Mo, K.; Mao, H.; Feldhoff, A.; Jiang, Z.; et al. A MOF Glass Membrane for Gas Separation. *Angew. Chem.* **2020**, *132*, 4395−4399.

(38) Bennett, T. D.; Horike, S. Liquid, Glass and Amorphous Solid States of Coordination Polymers and Metal−Organic Frameworks. *Nat. Rev. Mater.* **2018**, *3*, 431−440.

(39) Bennett, T. D.; Goodwin, A. L.; Dove, M. T.; Keen, D. A.; Tucker, M. G.; Barney, E. R.; Soper, A. K.; Bithell, E. G.; Tan, J.-C.; Cheetham, A. K. Structure and Properties of an Amorphous Metal-Organic Framework. *Phys. Rev. Lett.* **2010**, *104*, No. 115503.

(40) Tao, H.; Bennett, T. D.; Yue, Y. Melt-Quenched Hybrid Glasses from Metal−Organic Frameworks. *Adv. Mater.* **2017**, *29*, No. 1601705.

(41) Ma, N.; Horike, S. Metal−Organic Network-Forming Glasses. *Chem. Rev.* **2022**, *122*, 4163−4203.

(42) Xue, W. L.; Li, G. Q.; Chen, H.; Han, Y. C.; Feng, L.; Wang, L.; Gu, X. L.; Hu, S. Y.; Deng, Y. H.; Tan, L.; Dove, M. T.; Li, W.; Zhang, J.; Dong, H.; Chen, Z.; Deng, W. H.; Xu, G.; Wang, G.; Wan, C. Q. Melt-Quenched Glass Formation of a Family of Metal-Carboxylate Frameworks. *Nat. Commun.* **2024**, *15*, No. 2040.

(43) Zhang, W.; Liu, Y.; Jeppesen, H. S.; Pinna, N. Stöber Method to Amorphous Metal-Organic Frameworks and Coordination Polymers. *Nat. Commun.* **2024**, *15*, No. 5463.

(44) Xue, W. L.; Kolodzeiski, P.; Aucharova, H.; Vasa, S.; Koutsianos, A.; Pallach, R.; Song, J.; Frentzel-Beyme, L.; Linser, R.; Henke, S. Highly Porous Metal-Organic Framework Liquids and Glasses via a Solvent-Assisted Linker Exchange Strategy of ZIF-8. *Nat. Commun.* **2024**, *15*, No. 4420.

(45) Liu, C.; Wang, J.; Wan, J.; Cheng, Y.; Huang, R.; Zhang, C.; Hu, W.; Wei, G.; Yu, C. Amorphous Metal−Organic Framework-Dominated Nanocomposites with Both Compositional and Structural Heterogeneity for Oxygen Evolution. *Angew. Chem., Int. Ed.* **2020**, *59*, 3630−3637.

(46) Zhang, H.; Liu, S.; Zheng, A.; Wang, P.; Zheng, Z.; Wang, Z.; Cheng, H.; Dai, Y.; Huang, B.; Liu, Y. Enhanced Charge Transfer Process and Photocatalytic Activity over a Phosphonate-Based MOF via Amorphization Strategy. *Angew. Chem., Int. Ed.* **2024**, *63*, No. e202400965.

(47) Wu, H.; Huang, S.; Ding, F.; Ma, Y.; Zhai, Q.; Ren, Y.; Yang, Y.; Chen, L.; Tang, S.; Meng, X. Amorphous Bimetallic Metal−Organic Frameworks with an Optimized D-Band Center Enable Accelerating Oxygen Evolution Reaction. *J. Phys. Chem. C* **2022**, *126*, 19715−19725.

(48) Mitsuka, Y.; Ogiwara, N.; Mukoyoshi, M.; Kitagawa, H.; Yamamoto, T.; Toriyama, T.; Matsumura, S.; Haneda, M.; Kawaguchi, S.; Kubota, Y.; Kobayashi, H. Fabrication of integrated copper-based nanoparticles/amorphous metal−organic framework by a facile spray-drying method: highly enhanced CO2 hydrogenation activity for methanol synthesis. *Angew. Chem., Int. Ed.* **2021**, *60*, 22283−22288.

(49) Zeng, G.; Chen, D.; Zhen, C.; Feng, C.; Pang, Y.; He, W. Amorphous Fe-Phytate Enables Fast Polysulfide Redox for High-Loading Lithium−Sulfur Batteries. *Small* **2023**, *19*, No. 2302548.

(50) Bi, J.; Chen, L.; Yan, X.; Guo, J.; Tang, Y.; Jian, M.; Zhao, H. Amorphous Bimetallic-Organic Framework Enable Accelerated Redox Kinetics and Polysulfide Trapping for Lithium−Sulfur Batteries. *Chem. Eng. J.* **2024**, *496*, No. 154347.

(51) Zhang, X.; Li, G.; Zhang, Y.; Luo, D.; Yu, A.; Wang, X.; Chen, Z. Amorphizing Metal-Organic Framework Towards Multifunctional Polysulfide Barrier for High-Performance Lithium−Sulfur Batteries. *Nano Energy* **2021**, *86*, No. 106094.

(52) Elibol, M. K.; Jiang, L.; Xie, D.; Cao, S.; Pan, X.; Härk, E.; Lu, Y. Nickel Oxide Decorated Halloysite Nanotubes as Sulfur Host Materials for Lithium−Sulfur Batteries. *Global Challenges* **2023**, *7*, No. 2300005.

(53) Karaismailoglu, M.; Kutlu, S. Z.; Demir, T. U. *General Approach to Halloysite Clay Mineral*; Eckart, H. A., Ed.; Nova Science Publishers: New York, 2020; pp 1−16.

(54) Wang, Y.; Wang, X.; Ye, H.; Han, K. Carbon coated halloysite nanotubes as efficient sulfur host materials for lithium sulfur batteries. *Appl. Clay Sci.* **2019**, *179*, No. 105172.

(55) Li, J.; Sun, L.; Lv, G.; Liao, L. Application of clay minerals in lithium-sulfur batteries: A review. *J. Energy Chem.* **2025**, *106*, No. 114852.

(56) Li, R.; He, J.; Lei, M.; Yang, M.; Li, C. High-density catalytic heterostructures strung by buried-in carbon tube network as monolithic holey host for endurable Li-S batteries. *Chem. Eng. J.* **2022**, *446*, No. 137294.

(57) Liu, W.; Lei, M.; Zhou, X.; Li, C. Heterojunction interlocked catalysis-conduction network in monolithic porous-pipe scaffold for endurable Li-S batteries. *Energy Storage Mater.* **2023**, *58*, 74−84.

(58) Chen, K.; Qiu, W.; Wu, Q.; Zhou, X.; Liu, J.; Li, C. Tight bonding and high-efficiency utilization of S−S moieties to enable ultra-stable and high-capacity alkali-metal conversion batteries. *J. Mater. Chem. A* **2021**, *9*, 6160−6171.

(59) Zhang, W.; Bojdys, M. J.; Pinna, N. A Universal Synthesis Strategy for Tunable Metal-Organic Framework Nanohybrids. *Angew. Chem., Int. Ed.* **2023**, *62*, No. e202301021.

(60) Jodłowski, P. J.; Kurowski, G.; Dymek, K.; Jędrzejczyk, R. J.; Jeleń, P.; Gancarczyk, L.; Gancarczyk, A.; Węgrzynowicz, A.; Sawoszczuk, T.; Sitarz, M. In Situ Deposition of M (M = Zn; Ni; Co)-MOF-74 over Structured Carriers for Cyclohexene Oxidation—Spectroscopic and Microscopic Characterization. *Microporous Mesoporous Mater.* **2020**, *303*, No. 110249.

(61) Gao, Z.; Liang, L.; Zhang, X.; Xu, P.; Sun, J. Facile one-pot synthesis of Zn/Mg-MOF-74 with unsaturated coordination metal centers for efficient CO_2 adsorption and conversion to cyclic carbonates. *ACS Appl. Mater. Interfaces* **2021**, *13*, 61334−61345.

(62) Kadi, S.; Lellou, S.; Marouf-Khelifa, K.; Schott, J.; Gener-Batonneau, I.; Khelifa, A. Preparation, Characterisation and Application of Thermally Treated Algerian Halloysite. *Microporous Mesoporous Mater.* **2012**, *158*, 47−54.

(63) Xiao, L.; Wen, J.; Wu, G.; Chen, P.; Wang, M.; Jiang, H.; Zhou, X.; Yan, J. FeCo-MOF-74/Mn-MOF-74 Nanocomposite as a electrocatalyst for improved oxygen evolution reaction catalytic activity. *Fuel* **2025**, *381*, No. 133516.

(64) Wu, Q.; Mei, Y.; Huang, H.; Zhou, F.; Li, H.; Chen, H. Dynamic physical network constructed by tripartite H-bonds in artificial SEI to shape ultra-long-life dendrite-free lithium-metal anodes. *Mater. Today* **2024**, *75*, 112−124.

(65) Wu, Q.; Shadike, Z.; Xu, J.; Cao, F.; Li, C. Integrated reactor architecture of conductive network and catalytic nodes to accelerate polysulfide conversion for durable and high-loading Li-S batteries. *Energy Storage Mater.* **2023**, *55*, 73−83.

(66) Wu, Q.; Chen, K.; Shadike, Z.; Li, C. Relay-Type Catalysis by a Dual-Metal Single-Atom System in a Waste Biomass Derivative Host for High-Rate and Durable Li−S Batteries. *ACS Nano* **2024**, *18*, 13468−13483.

(67) Zhou, F.; Mei, Y.; Wu, Q.; Liu, J.; Chen, X.; Li, H.; Xu, J.; Chen, H. Lewis acid-optimized hydrolysable catalytic binder with dynamic hydrogen-bonded framework for durable lithium-sulfur batteries. *Chem. Eng. J.* **2025**, *507*, No. 160009.

(68) Li, C.; Wang, S.; Wang, Z.; Li, Z.; Zhang, C.; Ma, Y.; Shi, X.; Zhang, H.; Song, D.; Zhang, L. Investigation on the Necessity of Low Rates Activation toward Lithium-Sulfur Batteries. *Adv. Funct. Mater.* **2025**, *35*, No. 2414159.